Thermally induced fracture modeling during a long-term water injection

Yuhao Liu[a,b,c], Keita Yoshioka[c,d], Tao You[c,d], Hanzhang Li[a,b], Fengshou Zhang[a,b]

[a] *Key Laboratory of Geotechnical & Underground Engineering of Ministry of Education, Tongji University, Shanghai 200092, China*
[b] *Department of Geotechnical Engineering, College of Civil Engineering, Tongji University, Shanghai 200092, China*
[c] *Department Geoenergy, Montanuniversität Leoben, Leoben 8700, Austria*
[d] *Department of Environmental Informatics, Helmholtz Centre for Environmental Research - UFZ, Leipzig 04318, Germany*

Abstract

Significant volumes of water are injected into the subsurface for purposes such as maintaining reservoir pressure, enhancing production efficiency, or water disposal. In these operations, injection pressures are typically kept low to prevent the formation from fracturing. However, fractures may still be induced even at low injection pressures if the injected water cools the formation, causing thermal contraction. In this study, we numerically investigate thermally induced fractures during water injection using a variational thermo-hydro-mechanical phase-field model. Our simulation results show that cold water injection can nucleate multiple thermal fractures nearly orthogonal to a stimulated fracture, even if the injection pressure is below the fracturing pressure. Further simulation scenarios reveal that thermal fracture propagation is more likely with larger temperature differences, smaller in-situ stress anisotropy, and lower formation permeability. This study highlights the significant impact of thermal effects on fracture initiation and propagation, suggesting the need for careful consideration when regulating or managing fracture initiation during water injection.

Keywords: Thermal fracturing; Phase-field model; Thermo-hydro-mechanical coupling

1. Introduction

As injection fluid temperature is often cooler than that of the subsurface, thermal effects on the subsurface stress during water injection have been long recognized (Perkins and Gonzalez, 1985; Stephens and Voight, 1982). Large amounts of water injection or hydraulic fracturing process can generate substantial thermal stress and impact the critical pressure for fracturing (i.e., "frac pressure") or morphology of hydraulic fractures as demonstrated analytically (Enayatpour and Patzek, 2013; Perkins and Gonzalez, 1985), experimentally (Kumari et al., 2018; Li et al., 2020, 2021a; Liu et al., 2020b; Zhou et al., 2018), or numerically (Cheng et al., 2020; Feng et al., 2016; Hustedt et al., 2008; Qu et al., 2017; Ran et al., 2024; Tarasovs and Ghassemi, 2011; Zhang et al., 2015; Zhou et al., 2022). Unlike hydraulic fractures, which tend to propagate on the orthogonal plane to the minimum principal stress, thermal fractures may propagate in the parallel direction to the "original" minimum principal stress direction, branching from the existing hydraulic fractures once the local stress orientations are altered by the thermal effects as postulated by Perkins and Gonzalez (1985). Such branching may require substantial cooling of the rock (Enayatpour et al., 2019) or low-viscosity fluid, e.g., supercritical CO_2 (Li et al., 2018).

Compared to studies on thermal effects in hydraulic fracturing, less attention has been paid to low pressure water injection operation in geo-energy reservoirs (Kaya et al., 2011; Stefansson, 1997) or waterflooding (Sheng, 2014). Water injection usually operates with a lower rate (hence lower pressure) than hydraulic fracturing stimulation in permeable formations. Therefore, fractures are not considered to initiate or grow. However, with the presence of a near wellbore fracture, the prolonged injection period may induce tensile stress along the existing fracture, leading to eventual fracture initiation normal to the existing hydraulic fractures (Li et al., 2016c). Most works to date have focused on the thermal effects of water injection on the well performance (Bodvarsson, 1972; Martins et al., 1995; Shi et al., 2023), recovery efficiency (Liu et al., 2020a; Schroeder et al., 1982; Sun et al., 2019) and the risk of induced seismicity (Flóvenz et al., 2015; Gan and Elsworth, 2014; Parisio et al., 2019; Zang et al., 2014). Some studies investigated the deformation of fracture but assumed that the fracture propagation is limited on the plane normal to the minimum principal stress (Manchanda et al., 2019; Parisio and Yoshioka, 2020).

Numerical simulation is instrumental for predicting thermal fracturing behaviors over a long-term water injection (Yoshioka et al., 2019b). As numerical tools for thermal fracturing, two popular approaches are discrete and diffused methods. Li et al. (2016c) employed a discrete element method to simulate thermally induced microcracks in anisotropic thermal conductivity. Tomac and Gutierrez (2017) coupled a discrete element method with a bonded particle model to investigate the influence of fluid viscosity on fracture propagation. Yan et al. (2022) developed a novel two-dimensional finite discrete element method model and simulated the branching cracks along the main fracture in enhanced geothermal systems. A cohesive zone model has been proposed by Jiao et al. (2022) who combined it with a lattice boltzmann method and a discrete element method to study the synergistic effects of injected temperature difference and rock damage on fracture propagation. However, discrete approaches have disadvantages for fractures that coalesce or branch because such modeling requires a priori knowledge about the crack propagation path and complex remeshing strategy. For such complex thermal fracturing, the diffused approach is more appealing as it needs only one additional scalar field variable to represent fractures such as phase-field models (Zhuang et al., 2022). Phase-field models of fractures have been demonstrated as a rigorous approach to model brittle fracturing in the last couple of decades. Based on the pioneering work of Bourdin et al. (2000, 2008), the approach has been extended to poro-elastic media (Bourdin et al., 2012; Chukwudozie et al., 2019; Mikelić et al., 2015; Wheeler et al., 2014)), and then to thermo-poro-elastic media (Li et al., 2021b; Noii and Wick, 2019; Suh and Sun, 2021; Wang et al., 2023; Yi et al., 2024). However, no phase-field model has been applied to thermal fracturing over long-term low-rate injection as it requires more intricate coupling between the thermal, hydraulic, and mechanical processes.

In this study, we simulated thermally induced fractures during a long-term water injection, using our novel Thermo-Hydro-Mechanical (THM) phase-field method (Liu et al., 2024) with the two additional modifications. Firstly, we generalized the poroelastic degradation formulation, which depends not only on the phase-field (damage) but also on the energy decomposition scheme, to incorporate a no-tension energy decomposition (Freddi and Royer-Carfagni, 2010) to avoid compressive failure under in-situ stress conditions. Sedondly, we introduced the term contributed from the mechanical deformation in the energy conservation equation, which has non-negligible impacts in fractured regions. Our numerical simulations of low-pressure injection demonstrate that thermal cracks can nucleate in the direction nearly normal to the existing hydraulic fracture after days of injection with a certain degree of temperature difference. Furthermore, we observed that injection temperature, in-situ stress, and reservoir permeability affect thermal fracturing in morphology, pressure, and aperture. Our numerical simulations of thermal fracturing indicate that fracturing can occur even with low-pressure injection in highly permeable formations, which may have practical and regulatory implications in geoenergy operations.

This paper is structured as follows. Section 2 provides the governing equations for the thermo-hydro-mechanical variational phase-field modeling of hydraulic fracturing and the details of the no-tension decomposition method. The numerical implementation and workflow of the staggered scheme are illustrated in Section 3. Section 4 conducts a numerical parametric study about thermal fracturing during reinjection with different fracture patterns, and the results are discussed in Section 5. Final conclusions are drawn in Section 6.

We use the following notations throughout the paper. The second-order identity tensor is denoted by $\mathbf{I}$. The trace operator $\mathrm{Tr}(\cdot)$ acting on the second-order tensors $\mathbf{A}$ is defined as $\mathrm{Tr}(\mathbf{A}) = \boldsymbol{\delta} : \mathbf{A}$. $\nabla(\cdot)$ is the gradient of $(\cdot)$. A repeated index in subscript follows Einstein's summation convention i.e., $a_i b_i = a_1 b_1 + a_2 b_2 + a_3 b_3$ for i =1,2,3. However, this convention is ignored for an index in parentheses, e.g., $a_{(i)} b_{(i)}$.

2. Methods

2.1. Variational phase-field model for fracture

Fig.1 describes the existing crack set Γ in thermo-poroelastic medium Ω with the Dirichlet boundary $\partial_D\Omega$ and Neumann boundary $\partial_N\Omega$. Considering the body force $\mathbf{b}$ and traction $\bar{\mathbf{t}}$ on the outer boundary $\mathcal{C}_\mathrm{N}$, the Francfort-Marigo energy functional $\mathcal{E}$ (Francfort and Marigo, 1998) containing the discrete crack in Fig. 1a writes

$$\mathcal{E}(\varepsilon(\mathbf{u}), \mathit{\Gamma}) := \int_{\mathit{\Omega}\setminus\mathit{\Gamma}} \psi(\mathbf{u})\,\mathrm{d}V + \int_{\mathit{\Gamma}} G_c\,\mathrm{d}S, \tag{1}$$

where $\varepsilon(\mathbf{u})$ is the linearized strain defined as $\varepsilon = \frac{1}{2}(\nabla\mathbf{u} + \nabla^{\mathrm{T}}\mathbf{u})$ with $\mathbf{u}$ being the displacment, ψ is the strain energy density and G_c is the critical energy release rate, the energy required to create a fracture surface per unit area. With this definition of the total energy, Francfort and Marigo (1998) recast the Griffith's crack as a variational problem of:

$$(\mathbf{u}, \mathit{\Gamma}) = \underset{\mathbf{u},\mathit{\Gamma}}{\operatorname{argmin}}\ \mathcal{E}(\varepsilon(\mathbf{u}), \mathit{\Gamma}). \tag{2}$$

To alleviate the implementational difficulties of the discrete crack, we follow the regularization of Eq. (1) by Bourdin et al. (2000). As shown in Fig.1b, a phase-field variable υ is introduced that represents a state of the material from intact ($\upsilon = 1$) to fully broken ($\upsilon = 0$) and $\mathcal{E}$ is regularized as

$$\mathcal{E}_\ell(\varepsilon(\mathbf{u}), \upsilon) := \int_{\mathit{\Omega}} \psi(\mathbf{u}, \upsilon)\,\mathrm{d}V + \int_{\mathit{\Omega}} \frac{G_c}{4c_n}\left[\frac{(1-\upsilon)^n}{\ell} + \ell\nabla\upsilon\cdot\nabla\upsilon\right]\mathrm{d}V, \tag{3}$$

where c_n is the normalizing parameter defined as $c_n = \int_0^1 (1-s)^{n/2}\,\mathrm{d}S$ (Mesgarnejad et al., 2015; Tanné et al., 2018). For $n = 1$ and $n = 2$, the model is called $\mathtt{AT}_1$ model and $\mathtt{AT}_2$ model, respectively (Pham et al., 2011). Also, ℓ is the characteristic parameter with the dimension of a length that controls the phase-field profile transition. The generic form of strain energy density $\psi(\mathbf{u}, \upsilon)$ in Eq. (3) is defined as

$$\begin{aligned}\psi(\mathbf{u}, \upsilon) &= \frac{1}{2} g(\upsilon)\mathbb{C}_+ : \boldsymbol{\varepsilon} : \boldsymbol{\varepsilon} + \frac{1}{2}\mathbb{C}_- : \boldsymbol{\varepsilon} : \boldsymbol{\varepsilon} \\ &= \frac{1}{2}\mathbb{C}_{\text{eff}}(\upsilon) : \boldsymbol{\varepsilon} : \boldsymbol{\varepsilon},\end{aligned} \tag{4}$$

where

$$\mathbb{C}_{\text{eff}}(\upsilon) = g(\upsilon)\mathbb{C}_+ + \mathbb{C}_-, \tag{5}$$

with the degradation function $g(\upsilon)$[1]. Note the expression for $\mathbb{C}_{\text{eff}}$ depends on the energy decomposition scheme and $\psi(\mathbf{u}, \upsilon)$ acknowledges the phase-field variable υ and is continuous over Ω for integration.

2.2. Variational phase-field fracture model in thermo-poro-elastic medium

For the thermo-poro-elastic medium, the regularized functional can be extended to

$$\begin{aligned}\mathcal{F}(\varepsilon(\mathbf{u}), \upsilon, \zeta, T) := &\int_\Omega \psi_e(\mathbf{u}, T, \upsilon)\,\mathrm{d}V + \int_\Omega \psi_f(\mathbf{u}, \zeta, \upsilon)\,\mathrm{d}V + \int_\Omega \psi_T(T, \upsilon)\,\mathrm{d}V \\ &+ \int_\Omega \frac{G_c}{4c_n}\left[\frac{(1-\upsilon)^n}{\ell} + \ell\nabla\upsilon\cdot\nabla\upsilon\right]\mathrm{d}V.\end{aligned} \tag{6}$$

p and T represent the pressure and temperature field. The strain energy density ψ is assumed to be decomposed into elastic, hydraulic and thermal parts.

Denoting the elastic strain with $\boldsymbol{\varepsilon}_e$ and the thermal strain with $\boldsymbol{\varepsilon}_T$, the total strain is written as $\boldsymbol{\varepsilon} = \boldsymbol{\varepsilon}_e + \boldsymbol{\varepsilon}_T$, and the thermal strain is given by

$$\boldsymbol{\varepsilon}_T(\mathbf{u}) = \beta\Delta T\mathbf{I}, \tag{7}$$

where β is the thermal expansion coefficient. The elastic strain energy is then given as

$$\begin{aligned}\psi_e(\mathbf{u}, \upsilon, T) &= \frac{1}{2}\mathbb{C}_{\text{eff}}(\upsilon) : \boldsymbol{\varepsilon}_e : \boldsymbol{\varepsilon}_e \\ &= \frac{1}{2}\mathbb{C}_{\text{eff}}(\upsilon) : \Big(\boldsymbol{\varepsilon}(\mathbf{u}) - \beta\Delta T\mathbf{I}\Big) : (\boldsymbol{\varepsilon}(\mathbf{u}) - \beta\Delta T\mathbf{I})\,.\end{aligned} \tag{8}$$

The hydraulic energy of pore fluid is given as (Coussy, 2004; Li et al., 2021b; Yi et al., 2024)

$$\psi_f(\mathbf{u}, \upsilon, \zeta) = \frac{M_p}{2}\left[\alpha(\upsilon)\mathrm{Tr}(\varepsilon_{\mathbf{e}}) - \zeta\right]^2, \tag{9}$$

where $\alpha(\upsilon)$ and M_p are Biot's coefficient and modulus, and ζ is the incremental content of fluid. Without the thermal expansion effect, ζ writes (Biot, 1962; Mikelić et al., 2015)

$$\zeta = \alpha(\upsilon)\mathrm{Tr}(\boldsymbol{\varepsilon}_e) + \frac{p}{M_p}. \tag{10}$$

[1] In this study, we employed $g(\upsilon) = (1-k)\upsilon^2 + k$ where k is a phase-field parameter representing residual stiffness, which keeps the system of equations well-conditioned for the partly-broken state (Bourdin et al., 2000).

Following the formulation proposed in You and Yoshioka (2023), Biot's coefficient $\alpha(\upsilon)$ is

$$\alpha(\upsilon) = 1 - \frac{K_{\text{eff}}(\upsilon)}{K_s}, \tag{11}$$

where $K_{\text{eff}}(\upsilon)$ and K_s are the bulk moduli of effective media and solid grain. The effective bulk modulus does not only depend on υ but also on the type energy decomposition scheme applied. For the volumetric-deviatoric energy decomposition (Amor et al., 2009), the expression of K_{eff} is given in You and Yoshioka (2023), but the general expression of K_{eff} can also be obtained with the expression of $\mathbb{C}_{\text{eff}}(\upsilon)$ and spherical projection $\mathbf{P}_{\text{sph}} = \frac{1}{3}\mathbf{I}$ as

$$K_{\text{eff}}(\upsilon) = \frac{1}{9}\text{Tr}(\mathbf{P}_{\text{sph}} : \mathbb{C}_{\text{eff}}(\upsilon) : \mathbf{I}). \tag{12}$$

By defining the degradation coefficient g_k with the initial bulk modulus K as

$$g_k = K_{\text{eff}}(\upsilon)/K, \tag{13}$$

we can rewrite effective Biot's coefficient in Eq. (11) as

$$\alpha(\upsilon) = 1 - \frac{K_{\text{eff}}(\upsilon)}{K_s} = 1 - K_{\text{eff}}(\upsilon)\frac{1-\alpha_m}{K} = 1 - g_k(1-\alpha_m), \tag{14}$$

where α_m is the initial Biot's coefficient.

The thermal energy ψ_T is assumed to have no mechanical or hydraulic contribution and thus we have

$$\psi_T(T) = (\rho c)_m \left[(T - T_{\text{ref}}) - T\ln\left(\frac{T}{T_{\text{ref}}}\right)\right] \tag{15}$$

where T_{ref} is the reference temperature. $(\rho c)_m$ is the equivalent heat storage for porous medium given by

$$(\rho c)_m = \phi c_{p,f}\rho_f + (1-\phi)c_{p,s}\rho_s \tag{16}$$

where $c_{p,f}$ and $c_{p,s}$ are the specific heat of fluid and solid respectively, ρ is the density, and ϕ is the porosity. The total stress can be obtained by taking the derivative of $\mathcal{F}$ with respect to $\boldsymbol{\varepsilon}$ as

$$\sigma = \mathbb{C}_{\text{eff}}(\upsilon) : \varepsilon(\mathbf{u}) - \alpha(\upsilon)p\mathbf{I} - 3\beta K_{\text{eff}}(\upsilon)\Delta T\mathbf{I}. \tag{17}$$

The expression for $\mathbb{C}_{\text{eff}}$ is determined by the energy decomposition scheme. Among many energy decomposition schemes, most widely used models are volumetric-deviatoric model (Amor et al., 2009), no-tension model (Freddi and Royer-Carfagni, 2010) and spectral model (Miehe et al., 2010). In this study, we apply the no-tension model (see Appendix A for details), considering that the deep buried rock has a high compressive strength.

2.3. Mass transfer model

Considering the equivalent properties, the mass balance for a fracture-porous system is given as

$$\frac{\partial}{\partial t}\left(\alpha(\upsilon)\nabla\cdot\mathbf{u} + \frac{p}{M_p(\upsilon)} - \frac{T}{M_T(\upsilon)}\right) + \nabla\cdot(\mathbf{q}_f) = Q_f \quad \text{in} \quad \Omega, \tag{18}$$

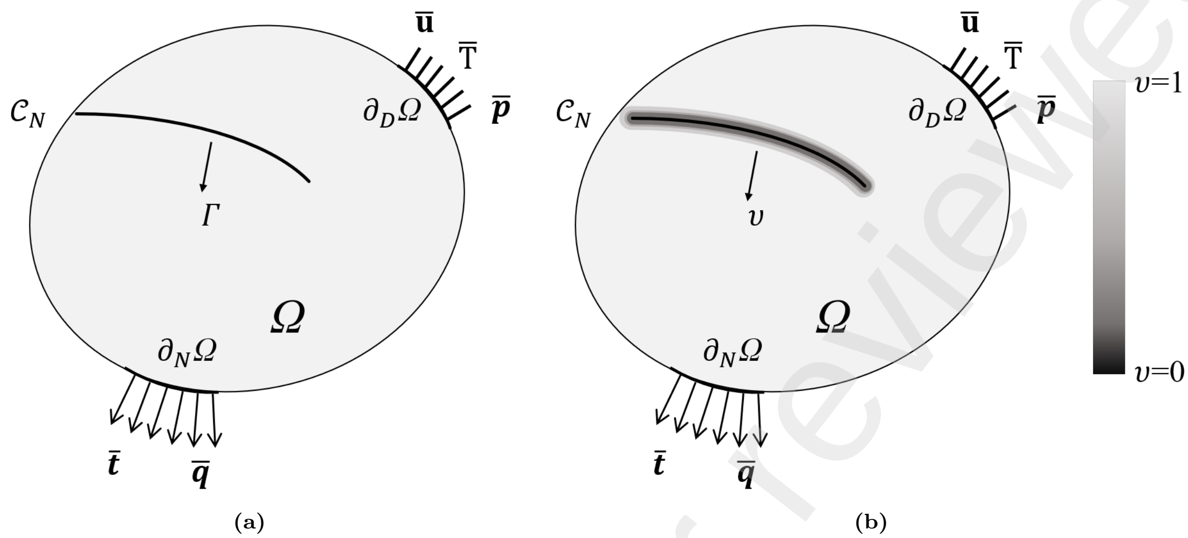

Fig. 1. Phase-field representation of (a) a discrete crack and (b) a diffused crack in thermo-poroelastic medium.

where $M_T(\upsilon)$ is the effective thermal storage coefficient that describes the thermal expansion in the incremental content of fluid and Q_f is the source term. We employ Darcy's law for the fluid flux $\mathbf{q}_f$:

$$\mathbf{q}_f = -\frac{\mathbf{K}}{\mu}\nabla(p+\gamma_f z) \quad \text{in} \quad \Omega, \tag{19}$$

with the permeability tensor $\mathbf{K}$, fluid viscosity μ, the specific body force γ_f and the vertical coordinate z. In fractures, an anisotropic permeability is applied with the enhancement taking into account the Poiseuille-type flow (Miehe and Mauthe, 2016; Miehe et al., 2015)

$$\mathbf{K} = \mathbf{K_m}\mathbf{I} + (1-\upsilon)^{\xi}\frac{\omega^2}{12}\left(\mathbf{I} - \mathbf{n}_\Gamma \otimes \mathbf{n}_\Gamma\right) \tag{20}$$

where $\mathbf{K_m}$ is the initial isotropic permeability, $\xi \geq 1$ is a weighting exponent You and Yoshioka (2023). In this study we apply $\xi = 50$. $\mathbf{n}_\Gamma$ is the normal vector along the interface. Moreover, the real fracture width ω is calculated by the maximum principal strain as

$$\omega = h_e \varepsilon_1. \tag{21}$$

Regarding the porosity update, we apply the equation from the work of Liu et al., 2024:

$$\phi(\varepsilon) = \phi + \varepsilon_1. \tag{22}$$

With the effective porosity in Eq. (22) and Biot's coefficient in Eq. (14), effective Biot's coefficient and average thermal expansion coefficient are updated as

$$\frac{1}{M_p(\upsilon,\varepsilon)} = \phi(\varepsilon)c_f + \frac{\alpha(\upsilon)-\phi(\varepsilon)}{K_s}, \tag{23}$$

$$\frac{1}{M_T(\upsilon,\varepsilon)} = \phi(\varepsilon)\alpha_f + 3\beta\left(\alpha(\upsilon) - \phi(\varepsilon)\right) \tag{24}$$

where c_f is the fluid compressibility, K_s is the solid phase's intrinsic bulk modulus, and α_f is the fluid volumetric thermal expansion coefficient.

2.4. Heat transfer model

The energy conservation in porous medium can be written (Li et al., 2016a):

$$3\beta K_{\text{eff}} T \frac{\partial(\nabla\cdot\mathbf{u})}{\partial t} + (\rho c)_m \frac{\partial T}{\partial t} + \nabla\cdot(\mathbf{q}_T) = Q_T, \tag{25}$$

where Q_T is the source term and $\mathbf{q}_T$ is the heat flux. The first term is the thermal effect due to the deformation, which was not included in our previous model (Liu et al., 2024), but has non-negligible impacts when the rock is fractured and experiences substantial deformation. We assume the local thermal equilibrium to unify the temperatures over Ω. $\mathbf{q}_T$ is composed of advective and conductive terms, and using Fourier's law we can write

$$\mathbf{q}_T = \rho_f \mathbf{q}_f c_f T - \lambda_{\text{eff}} \nabla T, \tag{26}$$

with effective thermal conductivity defined as

$$\lambda_{\text{eff}}(\varepsilon) = \phi(\varepsilon)\lambda_f + (1-\phi(\varepsilon))\lambda_s. \tag{27}$$

Also, the effective heat storage coefficient in Eq. (16) can now be rewritten as

$$(\rho c)_m(\varepsilon) = \phi(\varepsilon) c_{p,f}\rho_f + (1-\phi(\varepsilon)) c_{p,s}\rho_s. \tag{28}$$

Substituting Eq.(26) into Eq. (25), we have

$$3\beta K_{\text{eff}} T \frac{\partial(\nabla\cdot\mathbf{u})}{\partial t} + (\rho c)_m \frac{\partial T}{\partial t} + c_{p,f}\rho_f \mathbf{q}_f\cdot\nabla T - \nabla\cdot\lambda_{\text{eff}}\nabla T = Q_T. \tag{29}$$

3. Numerical implementation

The displacement $\mathbf{U}$ and phase-field υ are obtained from Eq.(6) by minimizing $\mathcal{F}$, which can be stated as

$$\begin{cases} (\mathbf{u}_i, \upsilon_i) = \operatorname{argmin}\left\{\mathcal{F}(\varepsilon(\mathbf{u}_i), \upsilon_i; \zeta, T) : \mathbf{u} \in \mathcal{U}(t_i), \upsilon \in \mathcal{V}(t_i, \upsilon_{i-1})\right\} \\ \mathcal{U}(t_i) = \left\{\mathbf{u} \in H^1(\Omega) : \mathbf{u} = 0 \quad \text{on} \quad \partial_N\Omega\right\} \\ \mathcal{V}(t_i, \upsilon_{i-1}) = \left\{\upsilon \in H^1(\Omega) : 0 \le \upsilon(x) \le \eta \;\; \forall x\right\} \end{cases}, \tag{30}$$

where

$$\eta = \begin{cases} 1 & \text{if} \quad \upsilon_{i-1}(x) \ge \upsilon_{ir} \\ \upsilon_{i-1}(x) & \text{otherwise} \end{cases}$$

and υ_{ir} is the irreversible threshold $\in [0,1]$ (e.g. 0.05). Because of the irreversibility, the phase-field needs to be solved with the inequality constraint, Eq. 30-3 (see You and Yoshioka (2023) for details). We follow an alternate minimization scheme proposed by Bourdin et al. (2000) where we minimize

$\mathcal{F}$ with respect to the displacement $\mathbf{u}$ while fixing the phase-field υ and then minimize $\mathcal{F}$ with respect to υ with fixed $\mathbf{u}$. Taking a directional derivative of Eq. (6) with respect to $\mathbf{u}$ ($\mathbf{w}_\mathbf{u} \in H^1$) and υ ($\mathbf{w}_\upsilon \in H^1$), we arrive at the weak forms of mechanical deformation and phase-field evolution:

$$\int_\Omega \nabla \mathbf{w}_u \cdot [\mathbb{C}_{\text{eff}} : \varepsilon_e - \alpha(\upsilon) p \mathbf{I}] \, \mathrm{d}V - \int_\Omega \mathbf{b} \cdot \mathbf{w}_u \, \mathrm{d}V - \int_{\mathcal{C}_N} \bar{\mathbf{t}} \cdot \mathbf{w}_u \, \mathrm{d}S = \mathbf{0} \tag{31}$$

$$\begin{aligned} &\int_\Omega \mathbf{w}_\upsilon \left[2(1-k)\upsilon\psi_+(\mathbf{u}) - \frac{p^2}{2}\frac{\partial 1/M_p(\upsilon)}{\partial \upsilon} \right] \mathrm{d}V - \int_\Omega \mathbf{w}_\upsilon \frac{G_c}{4c_n}\frac{n}{\ell}(1-\upsilon)^{n-1} \, \mathrm{d}V, \\ &- \int_{\mathcal{C}_N} \frac{G_c}{2c_n} \ell \nabla \mathbf{w}_\upsilon \cdot \nabla \upsilon \, \mathrm{d}V = \mathbf{0}. \end{aligned} \tag{32}$$

To solve for the pressure and temperature fields, we can derive the weak forms of mass and heat transfer equations with the variations $\mathbf{w}_p \in H^1$ and $\mathbf{w}_T \in H^1$ as

$$\begin{aligned} &\int_\Omega \frac{\partial}{\partial t}\left(\alpha(\upsilon)\nabla\cdot\mathbf{u} + \frac{1}{M_p(\upsilon,\varepsilon)}p - \frac{1}{M_T(\upsilon,\varepsilon)}T \right) \mathbf{w}_p \, \mathrm{d}V + \int_\Omega \frac{\mathbf{K}}{\mu}\nabla p \cdot \nabla \mathbf{w}_p \, \mathrm{d}V \\ &= \int_\Omega Q_f \mathbf{w}_p \, \mathrm{d}V - \int_{\mathcal{C}_\mathrm{N}} q_n \mathbf{w}_p \, \mathrm{d}S, \end{aligned} \tag{33}$$

and

$$\begin{aligned} &\int_\Omega (\rho c)_m(\varepsilon)\frac{\partial T}{\partial t}\mathbf{w}_T \, \mathrm{d}V + \int_\Omega \mathbf{w}_T c_f \rho_f \mathbf{q}_f \cdot \nabla T \, \mathrm{d}V + \int_\Omega \lambda_{\text{eff}}(\varepsilon)\nabla T \cdot \nabla \mathbf{w}_T \, \mathrm{d}V \\ &= \int_\Omega Q_T \mathbf{w}_T \, \mathrm{d}V - \int_{\mathcal{C}_\mathrm{N}} q_{Tn}\mathbf{w}_T \, \mathrm{d}S. \end{aligned} \tag{34}$$

For this four-field coupled problem i.e., Eqs. (31), (32), (33), (34), we employed a staggered scheme (Brun et al., 2020; Wang et al., 2009). The system is solved in a sequence of $\upsilon - (T - p - \mathbf{u})$ in which a global loop is set between υ and the sub-loop $(T - p - \mathbf{u})$ in the sub-loop, T, p and $\mathbf{u}$ are solved in a staggered manner. The time discretization of Eqs. 33 and 34 for the i^{th} iteration scheme of time step k is shown as

$$\begin{aligned} &\int_\Omega 3\beta K_{\text{eff}} T^{k,i} \frac{\varepsilon_{\text{vol}}(\mathbf{u}^{k,i-1}) - \varepsilon_{\text{vol}}(\mathbf{u}^{k-1})}{\Delta t}\mathbf{w}_T \, \mathrm{d}V + \int_\Omega (\rho c)_m(\varepsilon)\frac{T^{k,i} - T^{k-1}}{\Delta t}\mathbf{w}_T \, \mathrm{d}V \\ &+ \int_\Omega \mathbf{w}_T c_f \rho_f \mathbf{q}_f^{k,i-1} \cdot \nabla T \, \mathrm{d}V + \int_\Omega \lambda_{\text{eff}}(\varepsilon)\nabla T^{k,i} \cdot \nabla \mathbf{w}_T \, \mathrm{d}V = \int_\Omega Q_T \mathbf{w}_p \, \mathrm{d}V - \int_{\mathcal{C}_N} q_{Tn}\mathbf{w}_T \, \mathrm{d}S. \end{aligned} \tag{35}$$

with

$$\mathbf{q}_f^{k,i-1} = -\frac{\mathbf{K}}{\mu}\nabla p^{k,i-1} \tag{36}$$

and

$$\begin{aligned} &\int_\Omega \left(\alpha \frac{\varepsilon_{\text{vol}}(\mathbf{u}^{k,i}) - \varepsilon_{\text{vol}}(\mathbf{u}^{k-1})}{\Delta t} + \frac{1}{M_p}\frac{p^{k,i} - p^{k-1}}{\Delta t} - \frac{1}{M_T}\frac{T^{k,i} - T^{k-1}}{\Delta t}\right)\mathbf{w}_p dV + \int_\Omega \frac{\boldsymbol{K}}{\mu}\nabla p^{k,i} \cdot \nabla \mathbf{w}_p dV \\ &= \int_\Omega Q_f \mathbf{w}_p dV - \int_{\partial_N \Omega} q_n \mathbf{w}_p dS. \end{aligned} \tag{37}$$

To stabilize the sub-loop, we apply the fixed-stress splitting method by freezing the volumetric stress, we set

$$\begin{aligned}&K_{\text{eff}}\varepsilon_{\text{vol}}(\mathbf{u}^{k,i}) - \alpha p^{k,i} - 3\alpha_s K_{\text{eff}}(T^{k,i} - T_0)\\ &= K_{\text{eff}}\varepsilon_{\text{vol}}(\mathbf{u}^{k,i-1}) - \alpha p^{k,i-1} - 3\alpha_s K_{\text{eff}}(T^{k,i-1} - T_0).\end{aligned} \tag{38}$$

Thus, we have

$$\varepsilon_{\text{vol}}(\mathbf{u}^{k,i}) = \varepsilon_{\text{vol}}(\mathbf{u}^{k,i-1})\frac{\alpha}{K_{\text{eff}}}(p^{k,i} - p^{k,i-1}) + 3\alpha_s(T^{k,i} - T^{k,i-1}). \tag{39}$$

Then, substituting Eq. (39) into Eq. (37), we can eliminate the volumetric strain in the current iteration. The computational procedure is outlined in Algorithm 1, which has been implemented in an open-source code, OpenGeoSys (Bilke et al., 2023; Yoshioka et al., 2019a). The code has been verified in Liu et al. (2024) for hydraulic fractures in thermo-poroelastic media by one-dimensional Terzaghi's problem, one-dimensional thermal consolidation problem and the KGD hydraulic fracture propagation.

Algorithm 1 A staggered solution of THM phase-field modeling

Require: Tolerence: δ_υ, δ_T, δ_p, $\delta_{\mathbf{u}}$, maximum number of iteration for global loop $m^g_{\max}$, maximum number of iteration for subloop $m^s_{\max}$, total time step n etc.

Ensure: Displacement $\mathbf{u}$, temperature T, pressure p and phase-field υ.

for $k \leftarrow 1$ to n **do**
    /* Alternate minimization algorithm */
    while $\Delta\upsilon \geq \delta_\upsilon$ **and** $j \leq m^g_{\max}$ **do**

        $\upsilon^{k,j} = \textbf{Step\_}\upsilon(T^{k,j-1}, p^{k,j-1}, \mathbf{u}^{k,j-1})$;
        UpdateFractutreWidth$(\mathbf{u}, \upsilon)$;
        $\Delta\upsilon = |\upsilon^{k,j} - \upsilon^{k,j-1}|$; ▷ Solve Eq.(32)

        /* THM coupling algorithm */
        while $\Delta T \geq \delta_T$, $\Delta p \geq \delta_p$, $\Delta\mathbf{u} \geq \delta_{\mathbf{u}}$ **and** $i \leq m^s_{\max}$ **do**
            $T^{k,i} = \textbf{Step\_T}(p^{k,i}, \upsilon^{k,i})$; ▷ Solve Eq.(34)
            $\Delta T = |T^{k,i} - T^{k,i-1}|$;
            /* fixed stress splitting method with Eq.(39)*/
            $p^{k,i} = \textbf{Step\_p}(T^{k,i}, \mathbf{u}^{k,i-1}, p^{k,i-1}, \upsilon^{k,i})$; ▷ Solve Eq.(33)
            $\Delta p = |p^{k,i} - p^{k,j-i}|$;
            $\mathbf{u}^{k,i} = \textbf{Step\_u}(T^{k,i}, p^{k,i}, \upsilon^{k,i})$; ▷ Solve Eq.(31)
            UpdateFractutreWidth$(\mathbf{u}, \upsilon)$;
            $\Delta\mathbf{u} = |\mathbf{u}^{k,i} - \mathbf{u}^{k,i-1}|$;
            $i = i + 1$;
        end while

        $j = j + 1$;

    end while
end for

4. Thermal propagation during reinjection

This section presents a simulation study of the thermal fracture propagation for the five-spot pattern production scenario. Taking advantage of the symmetry, a quarter of the five-spot pattern was simulated where an injection well is located at the lower left corner while a production well is located at the upper right corner (Fig. 2). The initial reservoir temperature is 353.15K and cold water is injected into the reservoir with various degrees of temperature difference, $\Delta T = T_{\mathrm{res}} - T_{\mathrm{inj}}$, for 30 days while the producer maintains a constant bottom hole pressure at the initial reservoir pressure of 13 MPa. Because of the symmetry, the displacements in the normal direction are fixed at the left and bottom boundaries. Boundary loadings on the top and the right edges are applied to induce the stress of 20.5 MPa in the x-direction and 20 MPa in the y-direction. No flow boundary condition is applied at all the edges.

We consider that the injection well is hydraulically stimulated with a fracture length of 5m in the direction normal to the minimum stress (x-direction). Also, we assume that fractures will never heal (close) completely and assign a minimum fracture width of 3×10^{-5}m once nucleated. Other mechanical, thermal, and hydraulic parameters are listed in Table 1. We take into account a temperature-dependent fluid viscosity as with the following model (Magri et al., 2017):

$$\mu(T) = \mu_0 e^{-0.016\times(T-T_0)} \tag{40}$$

where $\mu_0 = 1$ cp and $T_0 = 293.15$K.

Table 1 Parameters for the reference case

Input parameters	Value	Unit
Young's modulus (E)	17	GPa
Poisson's ratio (v)	0.2	-
Critical surface energy release rate (G_c)	50	N/m
Biot coefficient (α_m)	0.9	-
Porosity (ϕ_m)	0.1	-
Reservoir permeability ($\mathbf{K_m}$)	100	md
Initial reservoir pressure	13	MPa
Initial reservoir temperature (T_{res})	353.15	K
Thermal conductivity of rock and fluid(λ)	3, 0.5	W/(m· K)
Thermal expansivity of rock (α_s)	1e-5	1/K
Specific heat capacity of rock and fluid ($c_{p,s}, c_{p,f}$)	800, 4200	J/(kg· K)
Injection rate (Q)	4.5e-3	m^3/s

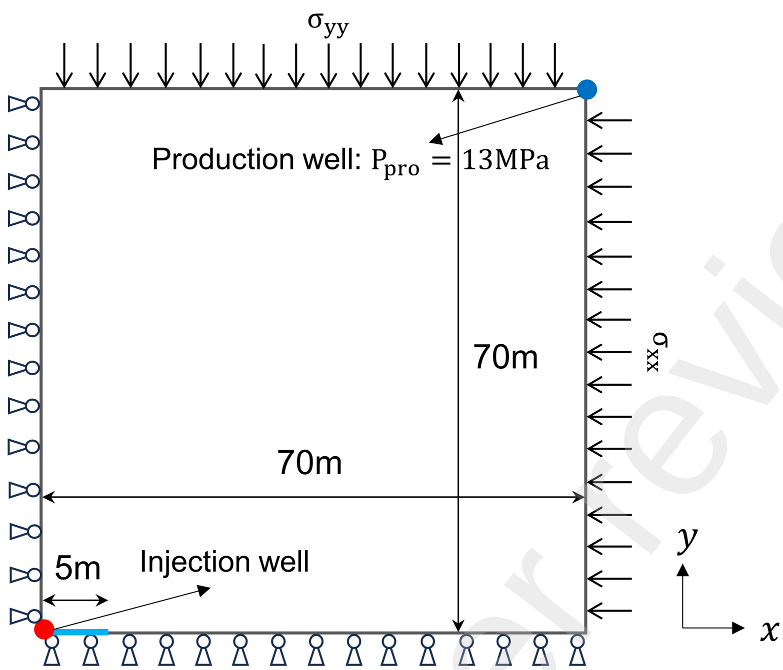

Fig. 2. Illustration of water flooding setup.

4.1. Sensitivity study

The following sub-sections present simulation results to study 4 different impacts: 1) temperature dependency of viscosity, 2) temperature difference, 3) in-situ stress anisotropy, and 4) formation permeability.

Temperature dependency of viscosity

We simulated two different scenarios to assess the impact of temperature dependency on viscosity: one with a constant water viscosity at the reservoir temperature of 353.15 K and the other with a temperature-dependent viscosity under the injection temperature of 313.15K (ΔT = 40K). Fig. 3 shows the induced fractures (phase-field profiles) after 30 days of injection. Several fractures nucleated and propagated. Thermal fractures are induced in the direction parallel to the minimum direction (y-direction), unlike hydraulic fractures. The water viscosity is high at a low temperature, but it decreases as it leaks into the warmer reservoir. If we neglect the temperature dependency of the water viscosity, the viscosity of injected water remains low and sustains fewer thermal cracks (Fig. 3b) and lower pressure in Fig. 3c. We consider this case with the temperature-dependent viscosity, the temperature difference of 40K, the stress differential of 0.5 MPa, and the reservoir permeability of 100 md as a reference case in the following analyses.

Temperature difference

Here, we present simulation results with ΔT = 30K, 40K, and 50K to study the impacts of the temperature difference on the fracture propagation. Thermal fractures are induced with ΔT = 40K and 50K but not with ΔT = 30K (Fig. 4), indicating that ΔT = 30K is not enough to induce

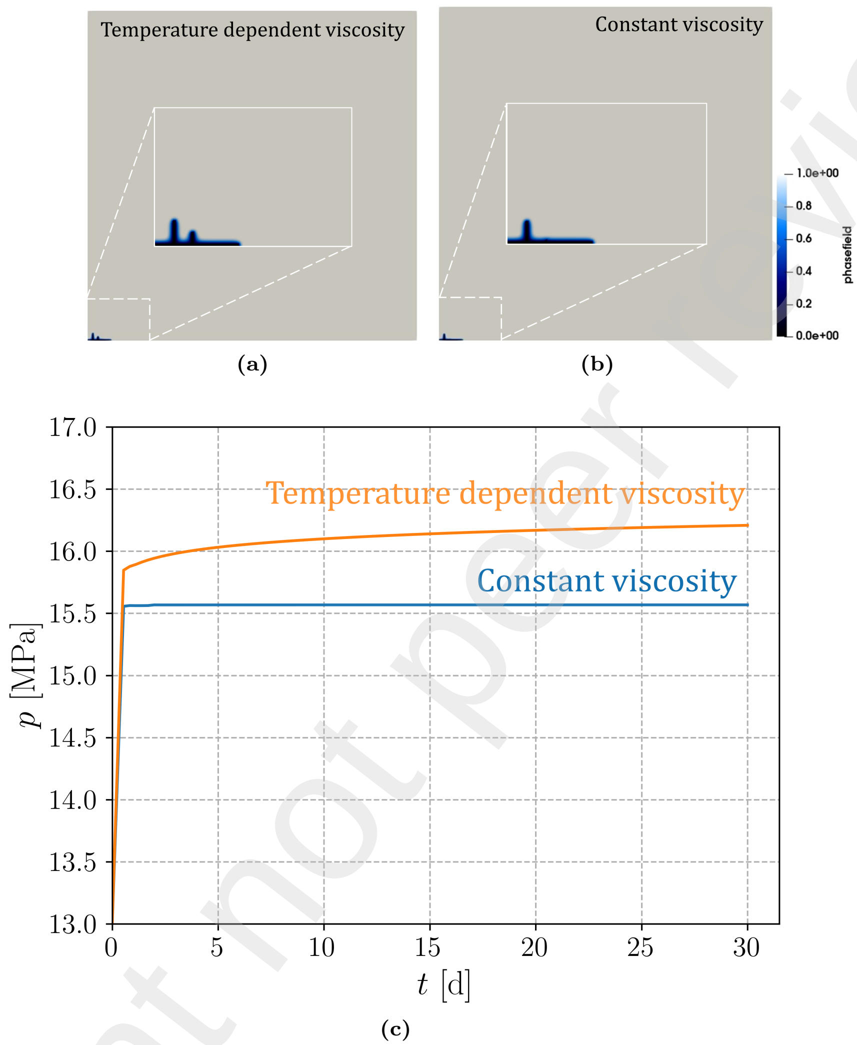

Fig. 3. Comparison between the fracturing cases of constant fluid viscosity and temperature-dependent fluid viscosity. (a) Fracture propagation under temperature-dependent fluid viscosity. (b) Fracture propagation under constant fluid viscosity. (c) Pressure at injection point under temperature-dependent and constant fluid viscosity.

the critical thermal contraction in this case. Also, for lower injection temperature (higher ΔT), the fluid viscosity is lower. And lower fluid viscosity increases the injection pressure, which can be seen in the results between $\Delta T = 40$K and 30K (Fig. 4c). However, higher pressure pressure also induces a larger number of thermal fractures and increases the fracture widths, which decreases the pressure. For this reason, the pressure responses from $\Delta T = 50$K and 40K are similar despite the lower viscosity for the $\Delta T = 50$K case.

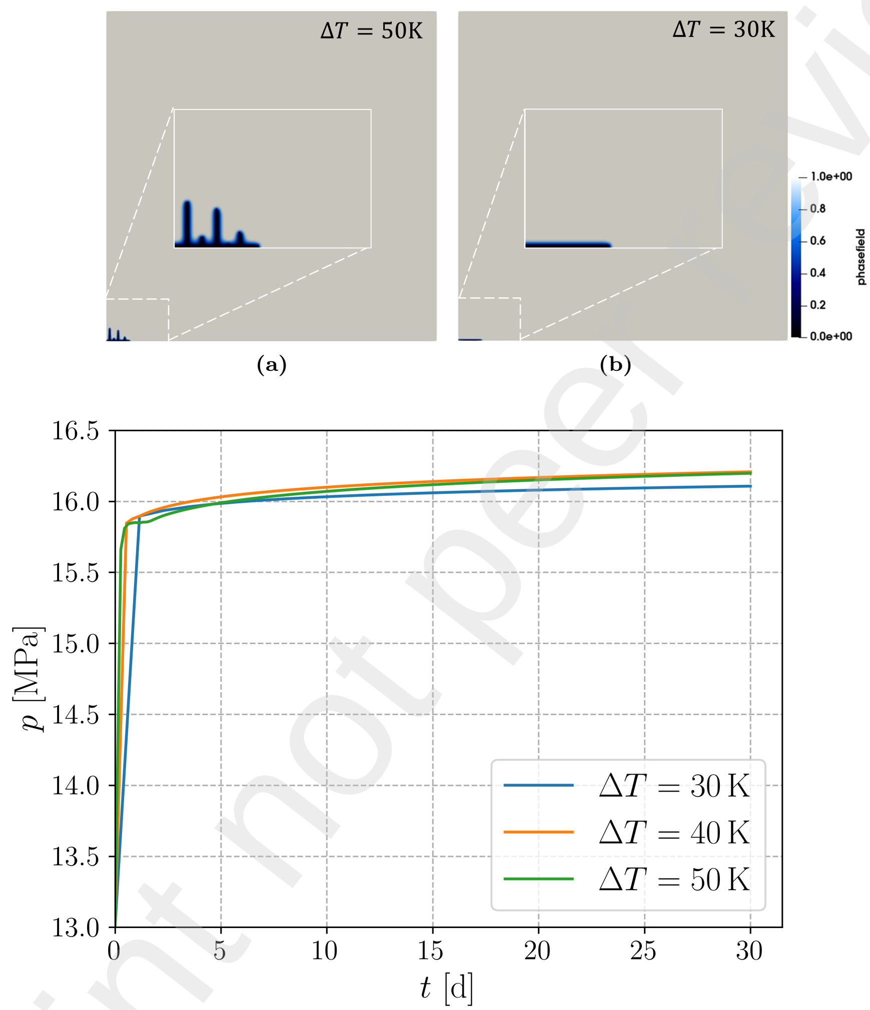

(a) (b) (c)

Fig. 4. Comparison between the fracturing cases under various temperature differences. (a) Fracture propagation under $\Delta T = 50$K. (b) Fracture propagation under $\Delta T = 30$K. (c) Pressure at injection point under $\Delta T = 50$, 40 and 30K.

In-situ stress anisotropy

This example analyzes thermal fracturing behaviors under different in-situ stress anisotropy. In addition to the reference case stress differential of 0.5 MPa, we consider the stress differential of 0 MPa and 1 MPa by changing the stress in the x-direction to 20 and 21 MPa. Fig. 5 shows that for higher stress differentials, it is more difficult to reverse the minimum principle stress around the main hydraulic fracture. Consequently, fewer and shorter thermal cracks nucleate along the main hydraulic fracture for higher stress differentials. As more thermal fractures nucleate with the isotropic stress case (0 MPs), the pressure at the injection point is slightly lower than the anisotropic cases (Fig. 5c). However, the stress differentials tested in this example overall do not have much impact on the evolution of pressure.

Formation permeability

Lastly, we simulated scenarios with different formation permeabilities of 80 md and 120 md in addition to the reference case of 100 md (Figs. 6a and 6b). At the same injection rate, a lower formation permeability imposes a higher injection pressure (Fig. 6c). Thus, more thermal fractures are induced by a higher injection pressure in a lower formation permeability, though the pressure responses do not exhibit clear indications of fracturing (e.g., pressure breakdowns). We note that the permeability is still high even for the “low” permeability case considered here (80 md), and that, while it is short, a fracture is still induced thermally in the high permeability formation of 120 md by water injection.

4.2. Fracture evolution

Through the sensitivity studies, we observed that the thermal process controls the nucleation, and the hydraulic process controls the propagation of fractures. In the reference case, multiple cracks nucleate first, and some of them outcompete the others (Fig. 7). Because a longer fracture receives more fluid, once a fracture grows longer than others, this fracture tends to grow even further.

If the stress differential is small, it is easier for these thermally induced fractures in the orthogonal direction to the principle minimum stress direction to grow. On the other hand, if the reservoir permeability is high, fluid leaks off to the formation, and the newly generated fractures do not retain enough fluid pressure to propagate further. This fluid leak-off is evidenced by the temperature profiles (Fig. 8). In the early time when fractures nucleate and grow, the formation temperature in the vicinity of the fractures is cooled (Fig. 8b), but over time a much wider region is cooled more uniformly (Fig. 8d).

The gradual dissipation of the local temperature gradient (Fig. 8) also leads to fracture closure as shown in the average fracture widths over time (Fig. 9), which has been also reported by experimental and numerical studies by (Lima et al., 2019; Petrova and Schmauder, 2015). The fractures close more quickly for the higher intermediate principle stress (or higher stress differential) as shown in Fig. 9a. For a higher reservoir permeability, the resultant lower injection pressure causes less fracture openings. However, for the case with $\mathbf{K_m} = 120$ md, fewer fractures are induced, and thus the average fracture opening is comparable to that of the $\mathbf{K_m} = 100$ md case (Fig. 9b). In all the cases, we see that the fractures eventually close to the prescribed minimum residual value ($3{\times}10^{-5}$m) as the temperature gradient dissipates locally.

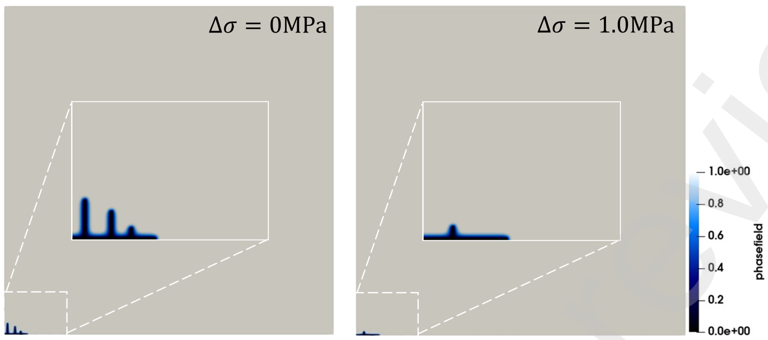

(a) **(b)**

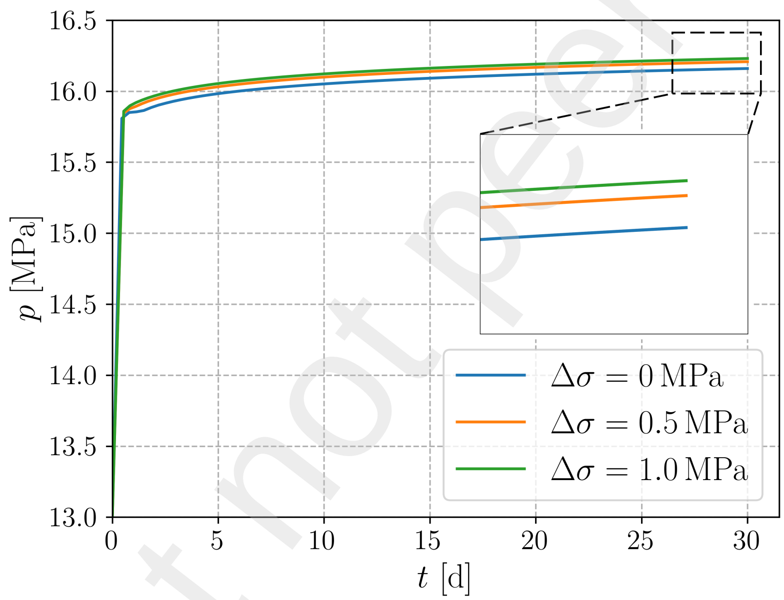

(c)

Fig. 5. Comparison between the fracturing cases under different in-situ stress. (a) Fracture propagation under $\Delta\sigma = 0$ MPa. (b) Fracture propagation under $\Delta\sigma = 1.0$ MPa. (c) Pressure at injection point under $\Delta\sigma = 0$, 0.5 and 1.0 MPa.

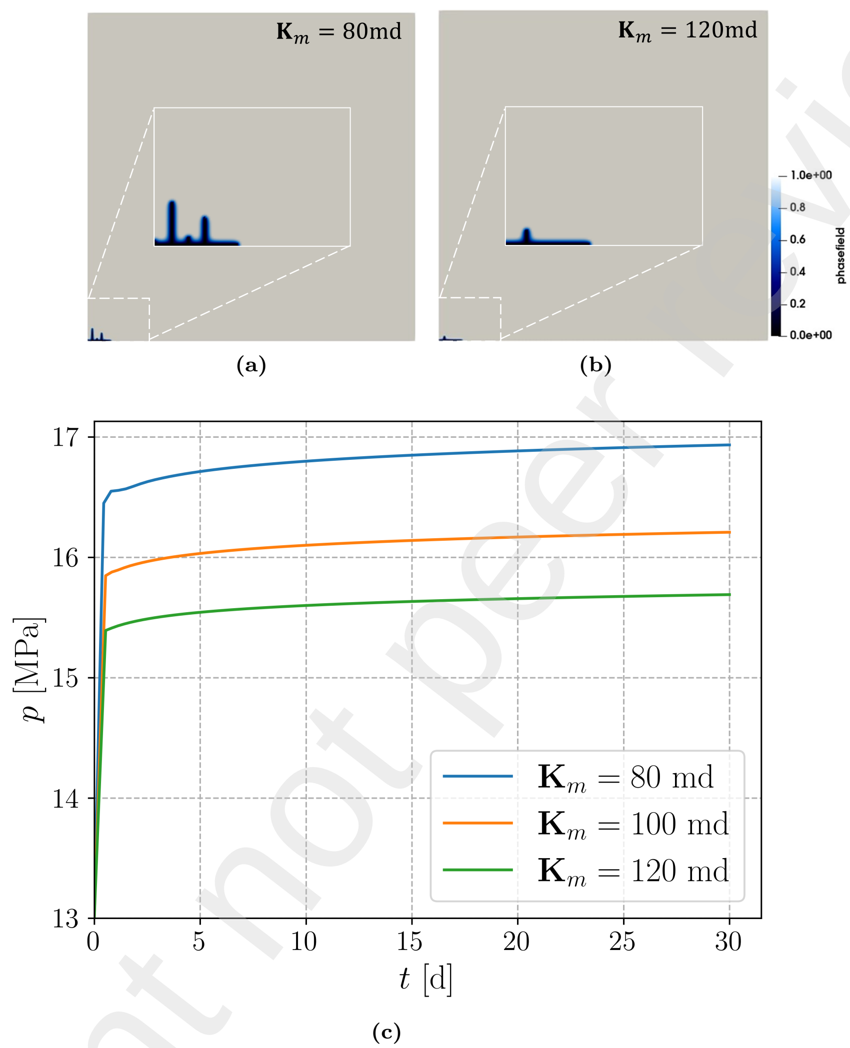

Fig. 6. Comparison between the fracturing cases under different formation permeabilities. (a) Fracture propagation under $\mathbf{K_m}$ = 80 md. (b) Fracture propagation under $\mathbf{K_m}$ = 120 md. (c) Pressure at injection point under $\mathbf{K_m}$ = 80, 100 and 120 md.

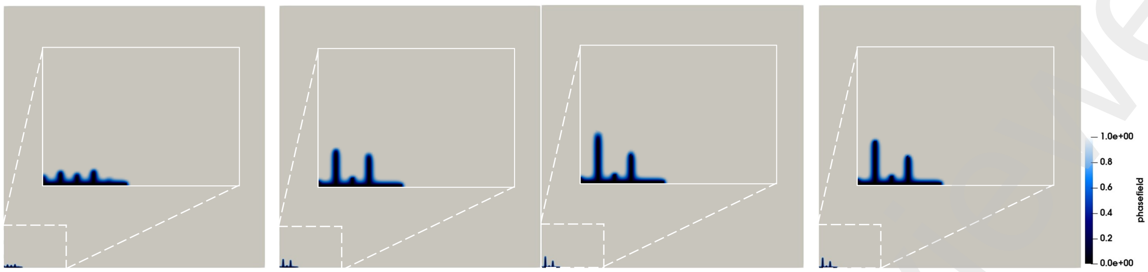

(a) t = 11 h. **(b)** t = 27.5 h. **(c)** t = 44 h. **(d)** t = 30 d.

Fig. 7. Fracture evolution in the case where $\mathbf{K_m} = 80$ md, $\Delta T = 40$ K and $\Delta\sigma = 0.5$ MPa.

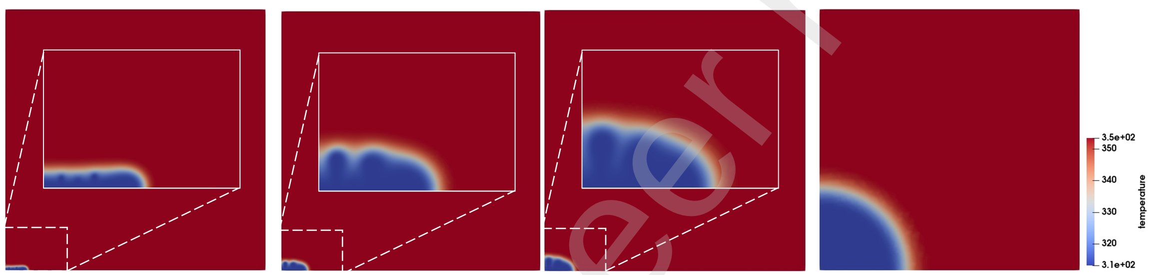

(a) t = 11 h. **(b)** t = 27.5 h. **(c)** t = 44 h. **(d)** t = 30 d.

Fig. 8. Thermal front evolution in the case where $\mathbf{K_m} = 80$ md, $\Delta T = 40$ K and $\Delta\sigma = 0.5$ MPa.

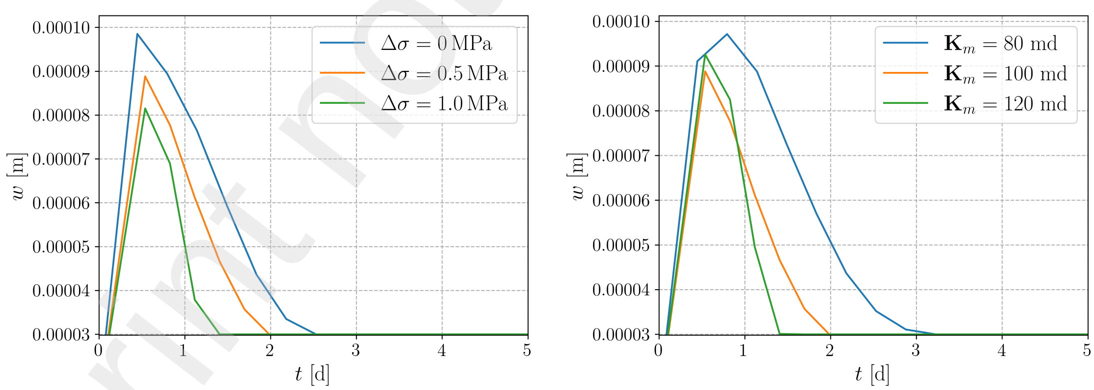

(a) **(b)**

Fig. 9. The evolution of the averaged opening of thermal fractures in the studies of (a) in-situ stress anisotropy and (b) formation permeability.

5. Discussion

Long-term water injection may fracture the reservoir formation even with high permeability and porosity. To initiate fracture under the confining stress, the fluid pressure must overcome the minimum principle stress and some tensile strength of the material. If we use the uniaxial tensile strength calculated by the masonry decomposition model with $\mathtt{AT}_1$ model Li et al. (2016b), we have:

$$p_b = \sigma_h + \sqrt{\frac{3G_c E(1-\nu)}{8\ell(1-2\nu)(1+\nu)}}. \tag{41}$$

Then, the critical pressure would be 21.33 MPa, with the properties used in this study, Based on this critical pressure, a regulatory injection pressure limit may be set to 90% (19.2 MPa). In all of our cases studied, however, the pressures never exceed this value, and thermal fractures are still induced in some cases.

The thermal fractures are developed in our simulations, where thermal conduction with intense convection from injection creates a large temperature gradient around the existing hydraulic fracture, inducing enough thermal tensile stress to initiate fractures. Other works reported that thermal stress enhances the propagation of hydraulic fractures during injection, but few analyzed the possibility of a new set of thermal fracture nucleation due to the modeling limitation on a number of propagating fractures or fracture directions (Parisio et al., 2019; Parisio and Yoshioka, 2020). Without such modeling limitations on fracture propagation, we were able to analyze the possibility of thermal fracturing.

Our analyses indicate that, even if the injection pressure remains lower than the critical pressure, formation fracturing is possible in practical scenarios of water injection into high permeable formations cases such as geothermal doublet systems or water flooding. Furthermore, injection pressure does not exhibit a sudden pressure drop, which is typically detected in hydraulically induced fracturing. Thus, detecting the onset or propagation of thermal fracturing may be difficult, if not impossible, from monitoring the pressure responses alone. This presents a significant challenge for operators and regulators, requiring additional monitoring measures, such as acoustic emission sensors if the objective is to prevent the fracturing of the formation entirely.

In this study, we assumed a minimum residual fracture width. This assumption may only be reasonable for investigating the propagation of thermal fractures However, for production performance analyses, one may need a more elaborated treatment of residual fracture width (e.g., reduced fracture stiffness) as some studies have reported that the changing hydraulic and heat transfer properties in unpropped fractures can affect production and the production may in turn induce the fracture closure with the pressure depletion(Lee et al., 2016; Shu et al., 2020; Wei et al., 2024). Additionally, our model is currently limited to single-phase flow. For other geoenergy applications, such as water flooding or CO2 storage, understanding how injected fluids diffuse in the presence of thermal fractures is crucial. Future studies could extend our simulation scenarios to higher reservoir temperature conditions, such as supercritical geothermal systems, where complex fluid phase transitions occur. It would also be valuable to consider the interaction between natural faults and secondary fractures in deep reservoirs, as some studies suggest a potential link between fracture reactivation and induced seismicity (Rutqvist et al., 2013; Wassing et al., 2014).

6. Conclusions

This paper investigated thermal fracturing during a long-term water injection. We used a quarter model to simulate a five-spot pattern of water injected into a high-permeability reservoir. From our simulations, we can draw the following conclusions:

1. Fractures can be induced even in high-permeability formation even without exceeding the critical fracture pressure as long as a sufficiently large temperature difference is provided.
2. More thermally induced fractures propagate when in-situ stress differentials are lower, or when the in-situ stress is more isotropic.
3. The occurrence of thermal fractures leaves no discernible impact on pressure responses, making fracture detection nearly impossible and potentially necessitating additional geophysical monitoring programs.
4. In the high-permeability formations considered in this study, induced fractures gradually close over time, and their hydraulic contributions diminish.

Declaration of competing interest

The authors declare that they have no known competing financial interests or personal relationships that could have appeared to influence the work reported in this paper.

Data availability

No data was used for the research described in the article.

Acknowledgement

This work is supported by the National Key Research and Development Project (No.2023YFE0110900) and National Natural Science Foundation of China (No.42320104003, 42077247, 12202137).

Appendix A. Implementional details of the no-tension model in 3D

In the no-tension model, the strain is decomposed so that the positive strain ($\boldsymbol{\varepsilon}_+$) is a positive definite tensor and is coaxial with $\boldsymbol{\varepsilon}$. Let $(\varepsilon_1, \varepsilon_2, \varepsilon_3)$ be a spectral decomposition of $\boldsymbol{\varepsilon}$ such that $\varepsilon_1 \geq \varepsilon_2 \geq \varepsilon_3$. Then we have

$$\boldsymbol{\varepsilon} = \sum_{i=1}^{3} \varepsilon_i \boldsymbol{n}_{(i)} \otimes \boldsymbol{n}_{(i)} := \varepsilon_i \boldsymbol{M}_i, \tag{A.1}$$

where $\boldsymbol{n}_{(i)}$ represents an eigenvector. Then the positive and the negative strains are

$$\boldsymbol{\varepsilon}_+ = \sum_{i=1}^{3} a_i \boldsymbol{n}_{(i)} \otimes \boldsymbol{n}_{(i)} = a_i \boldsymbol{M}_i, \quad \boldsymbol{\varepsilon}_- = \sum_{i=1}^{3} b_i \boldsymbol{n}_{(i)} \otimes \boldsymbol{n}_{(i)} = b_i \boldsymbol{M}_i, \tag{A.2}$$

where $a_i = \frac{\varepsilon_i + |\varepsilon_i|}{2}$ and $b_i = \varepsilon_i - a_i$ so that $\boldsymbol{\varepsilon} = \boldsymbol{\varepsilon}_+ + \boldsymbol{\varepsilon}_-$. Then the positive and negative strain energy densities are given by:

$$\psi_+ = \frac{\lambda}{2} (\mathrm{Tr}\,(\boldsymbol{\varepsilon}_+))^2 + \mu \boldsymbol{\varepsilon}_+ : \boldsymbol{\varepsilon}_+, \tag{A.3}$$

and

$$\psi_- = \frac{\lambda}{2}(\mathrm{Tr}\,(\boldsymbol{\varepsilon}_-))^2 + \mu\boldsymbol{\varepsilon}_- : \boldsymbol{\varepsilon}_-. \tag{A.4}$$

In the original work of Freddi and Royer-Carfagni (2010), the implementational details (e.g. tangential stiffness tensors) are not available, and also their implementations are in 2D. In the followings, we derive the implementation details in 3D.

According to the strain energy definitions, the corresponding stresses can be obtained[2] as

$$\begin{aligned}\boldsymbol{\sigma}_+ = \frac{\partial\psi_+}{\partial\boldsymbol{\varepsilon}} = \frac{\partial\psi_+}{\partial\varepsilon_i}\mathbf{M}_i = \frac{\partial\psi_+}{\partial a_k}\frac{\partial a_k}{\partial\varepsilon_i}\mathbf{M}_i \\ = \sum_k \left(\lambda\mathrm{Tr}\,(\boldsymbol{\varepsilon}_+) + 2\mu a_{(k)}\right)\alpha_{(k)i}\mathbf{M}_i := f_i\mathbf{M}_i\end{aligned} \tag{A.5}$$

and

$$\begin{aligned}\boldsymbol{\sigma}_- = \frac{\partial\psi_-}{\partial\boldsymbol{\varepsilon}} = \frac{\partial\psi_-}{\partial\varepsilon_i}\mathbf{M}_i = \frac{\partial\psi_-}{\partial b_k}\frac{\partial b_k}{\partial\varepsilon_i}\mathbf{M}_i \\ = \sum_k \left(\lambda\mathrm{Tr}\,(\boldsymbol{\varepsilon}_-) + 2\mu b_{(k)}\right)\beta_{(k)i}\mathbf{M}_i := g_i\mathbf{M}_i\end{aligned} \tag{A.6}$$

where

$$\alpha_{ki} = \frac{\partial a_k}{\partial\varepsilon_i}, \quad \text{and} \quad \beta_{ki} = \frac{\partial b_k}{\partial\varepsilon_i}.$$

The tangential stiffness tensors can be obtained by taking a derivative of the stress tensors as

$$\begin{aligned}\mathbb{C}_+ = \frac{\partial\boldsymbol{\sigma}_+}{\partial\boldsymbol{\varepsilon}} = \frac{\partial f_i}{\partial\varepsilon_j}\mathbf{M}_i\otimes\mathbf{M}_j + h_{+,ij}\mathbf{M}_i\odot\mathbf{M}_j \\ = (\lambda + 2\mu\delta_{kl})\alpha_{li}\alpha_{kj}\mathbf{M}_i\otimes\mathbf{M}_j + h_{+,ij}\mathbf{M}_i\odot\mathbf{M}_j\end{aligned} \tag{A.7}$$

and

$$\begin{aligned}\mathbb{C}_- = \frac{\partial\boldsymbol{\sigma}_-}{\partial\boldsymbol{\varepsilon}} = \frac{\partial g_i}{\partial\varepsilon_j}\mathbf{M}_i\otimes\mathbf{M}_j + h_{-,ij}\mathbf{M}_i\odot\mathbf{M}_j \\ = (\lambda + 2\mu\delta_{kl})\beta_{li}\beta_{kj}\mathbf{M}_i\otimes\mathbf{M}_j + h_{-,ij}\mathbf{M}_i\odot\mathbf{M}_j\end{aligned} \tag{A.8}$$

where

$$\begin{aligned}\frac{\partial f_i}{\partial\varepsilon_j} = \frac{\partial f_i}{\partial a_k}\alpha_{kj} = \alpha_{kj}\frac{\partial}{\partial a_k}\left(\lambda\mathrm{Tr}\,(\boldsymbol{\varepsilon}_+) + 2\mu a_m\right)\alpha_{mi} \\ = \sum_k\sum_l \alpha_{(l)i}\alpha_{(k)j}\left(\lambda + 2\mu\delta_{(k)(l)}\right),\end{aligned} \tag{A.9}$$

$$\begin{aligned}\frac{\partial g_i}{\partial\varepsilon_j} = \frac{\partial g_i}{\partial b_k}\beta_{kj} = \beta_{kj}\frac{\partial}{\partial b_k}\left(\lambda\mathrm{Tr}\,(\boldsymbol{\varepsilon}_-) + 2\mu b_m\right)\beta_{mi} \\ = \sum_k\sum_l \beta_{(l)i}\beta_{(k)j}\left(\lambda + 2\mu\delta_{(k)(l)}\right),\end{aligned} \tag{A.10}$$

[2] We refer to Silhavy (1997) for the derivatives of scalar and tensor valued functions with respect to a scalar or tensor used in this Appendix.

$$h_{+,ij} = \begin{cases} \dfrac{f_{(i)} - f_{(j)}}{\varepsilon_{(i)} - \varepsilon_{(j)}} = \dfrac{\left(\lambda \mathrm{Tr}\left(\varepsilon_{+}\right) + 2\mu a_k\right)\left(\alpha_{k(i)} - \alpha_{k(j)}\right)}{\varepsilon_{(i)} - \varepsilon_{(j)}} & \text{if } \varepsilon_{(i)} \neq \varepsilon_{(j)} \\ \dfrac{\partial f_{(i)}}{\partial \varepsilon_{(i)}} - \dfrac{\partial f_{(j)}}{\partial \varepsilon_{(i)}} = \left(\lambda + 2\mu\delta_{kl}\right)\alpha_{k(i)}\left(\alpha_{l(i)} - \alpha_{l(j)}\right) & \text{if } \varepsilon_{(i)} = \varepsilon_{(j)} \\ 0 & \text{if } i = j \end{cases}, \tag{A.11}$$

and

$$h_{-,ij} = \begin{cases} \dfrac{g_{(i)} - g_{(j)}}{\varepsilon_{(i)} - \varepsilon_{(j)}} = \dfrac{\left(\lambda \mathrm{Tr}\left(\varepsilon_{-}\right) + 2\mu b_k\right)\left(\beta_{k(i)} - \beta_{k(j)}\right)}{\varepsilon_{(i)} - \varepsilon_{(j)}} & \text{if } \varepsilon_{(i)} \neq \varepsilon_{(j)} \\ \dfrac{\partial g_{(i)}}{\partial \varepsilon_{(i)}} - \dfrac{\partial g_{(j)}}{\partial \varepsilon_{(i)}} = \left(\lambda + 2\mu\delta_{kl}\right)\beta_{k(i)}\left(\beta_{l(i)} - \beta_{l(j)}\right) & \text{if } \varepsilon_{(i)} = \varepsilon_{(j)} \\ 0 & \text{if } i = j \end{cases}. \tag{A.12}$$

The decomposition of the positive and the negative strains is described in Sacco (1990) and summarized in Algorithm 2. Accordingly, all the necessary coefficients, α_{ij} and β_{ij} are:

$$\begin{aligned} \alpha_{11} &= H_1 + (1 - H_1)H_2 + (1 - H_1)(1 - H_2)H_3, \\ \alpha_{12} &= \frac{\nu}{1 - \nu}(1 - H_1)(1 - H_2)H_3, \\ \alpha_{13} &= \nu(1 - H_1)H_2 + \frac{\nu}{1 - \nu}(1 - H_1)(1 - H_2)H_3, \end{aligned}$$

$$\begin{aligned} &\alpha_{21} = 0, && \alpha_{22} = H_1 - (1 - H_1)H_2, && \alpha_{23} = \nu(1 - H_1)H_2, \\ &\alpha_{31} = 0, && \alpha_{32} = 0, && \alpha_{33} = H_1, \end{aligned}$$

$$\begin{aligned} &\beta_{11} = 1 - \alpha_{11}, && \beta_{12} = -\alpha_{12}, && \beta_{13} = -\alpha_{13}, \\ &\beta_{21} = -\alpha_{21}, && \beta_{22} = 1 - \alpha_{22}, && \beta_{23} = -\alpha_{23}, \\ &\beta_{31} = -\alpha_{31}, && \beta_{32} = -\alpha_{32}, && \beta_{33} = 1 - \alpha_{33}, \end{aligned}$$

where

$$H_1 = H\left(\varepsilon_3\right), \quad H_2 = H\left(\varepsilon_2 + \nu\varepsilon_3\right), \quad H_3 = H\left((1 - \nu)\epsilon_1 + \nu(\varepsilon_2 + \varepsilon_3)\right).$$

References

Amor, H., Marigo, J.-J., and Maurini, C. (2009). Regularized formulation of the variational brittle fracture with unilateral contact: Numerical experiments. *Journal of the Mechanics and Physics of Solids*, 57(8):1209–1229.

Algorithm 2 Masonry-like model

Perform a spectral decomposition $\varepsilon = (\varepsilon_1, \varepsilon_2, \varepsilon_3)$ so that $\varepsilon_1 \geq \varepsilon_2 \geq \varepsilon_3$
if $\varepsilon_3 \geq 0$ **then**
    $\varepsilon_+ \leftarrow \varepsilon$
else if $\varepsilon_2 + \nu\varepsilon_3 \geq 0$ **then**
    $\varepsilon_+ \leftarrow (\varepsilon_1 + \nu\varepsilon_3, \varepsilon_2 + \nu\varepsilon_3, 0)$
else if $(1-\nu)\varepsilon_1 + \nu(\varepsilon_2 + \varepsilon_3) \geq 0$ **then**
    $\varepsilon_+ \leftarrow (\varepsilon_1 + \frac{\nu}{1-\nu}(\varepsilon_2 + \varepsilon_3), 0, 0)$
else
    $\varepsilon_+ \leftarrow 0$
end if

Bilke, L., Lehmann, C., Naumov, D., Fischer, T., Wang, W., Buchwald, J., Rink, K., Grunwald, N., Zill, F., Kiszkurno, F. K., Mollali, M., Nagel, T., Thiedau, J., Gerasimov, T., Ziaei Rad, V., Kurgyis, K., Lu, R., Silbermann, C., Heinze, J., Vehling, F., Meng, B., Yoshioka, K., You, T., Chaudhry, A., Shao, H., Günther, L., Kantzenbach, M., Kolditz, O., and Meisel, T. (2023). Opengeosys.

Biot, M. A. (1962). Mechanics of deformation and acoustic propagation in porous media. *Journal of applied physics*, 33(4):1482–1498.

Bodvarsson, G. (1972). Thermal problems in the siting of reinjection wells. *Geothermics*, 1(2):63–66.

Bourdin, B., Chukwudozie, C., and Yoshioka, K. (2012). A variational approach to the numerical simulation of hydraulic fracturing. In *SPE Annual Technical Conference and Exhibition*, pages SPE–159154.

Bourdin, B., Francfort, G. A., and Marigo, J.-J. (2000). Numerical experiments in revisited brittle fracture. *Journal of the Mechanics and Physics of Solids*, 48(4):797–826.

Bourdin, B., Francfort, G. A., and Marigo, J.-J. (2008). The variational approach to fracture. *Journal of elasticity*, 91:5–148.

Brun, M. K., Ahmed, E., Berre, I., Nordbotten, J. M., and Radu, F. A. (2020). Monolithic and splitting solution schemes for fully coupled quasi-static thermo-poroelasticity with nonlinear convective transport. *Computers & Mathematics with Applications*, 80(8):1964–1984.

Cheng, Y., Zhang, Y., Yu, Z., Hu, Z., and Yang, Y. (2020). An investigation on hydraulic fracturing characteristics in granite geothermal reservoir. *Engineering Fracture Mechanics*, 237:107252.

Chukwudozie, C., Bourdin, B., and Yoshioka, K. (2019). A variational phase-field model for hydraulic fracturing in porous media. *Computer Methods in Applied Mechanics and Engineering*, 347:957–982.

Coussy, O. (2004). *Poromechanics*. John Wiley & Sons.

Enayatpour, S. and Patzek, T. (2013). Thermal shock in reservoir rock enhances the hydraulic fracturing of gas shales. In *SPE/AAPG/SEG Unconventional Resources Technology Conference*, pages URTEC–1620617. URTeC.

Enayatpour, S., van Oort, E., and Patzek, T. (2019). Thermal cooling to improve hydraulic fracturing efficiency and hydrocarbon production in shales. *Journal of Natural Gas Science and Engineering*, 62:184–201.

Feng, W., Were, P., Li, M., Hou, Z., and Zhou, L. (2016). Numerical study on hydraulic fracturing in tight gas formation in consideration of thermal effects and thm coupled processes. *Journal of Petroleum Science and Engineering*, 146:241–254.

Flóvenz, Ó. G., Ágústsson, K., Gudnason, E. Á., and Kristjánsdóttir, S. (2015). Reinjection and induced seismicity in geothermal fields in iceland. In *Proceedings world geothermal congress*, pages 19–25.

Francfort, G. A. and Marigo, J.-J. (1998). Revisiting brittle fracture as an energy minimization problem. *Journal of the Mechanics and Physics of Solids*, 46(8):1319–1342.

Freddi, F. and Royer-Carfagni, G. (2010). Regularized variational theories of fracture: a unified approach. *Journal of the Mechanics and Physics of Solids*, 58(8):1154–1174.

Gan, Q. and Elsworth, D. (2014). Analysis of fluid injection-induced fault reactivation and seismic slip in geothermal reservoirs. *Journal of Geophysical Research: Solid Earth*, 119(4):3340–3353.

Hustedt, B., Zwarts, D., Bjoerndal, H.-P., Masfry, R., and van den Hoek, P. J. (2008). Induced Fracturing in Reservoir Simulations: Application of a New Coupled Simulator to a Waterflooding Field Example. *SPE Reservoir Evaluation & Engineering*, 11(03):569–576.

Jiao, K., Han, D., Wang, D., Chen, Y., Li, J., Gong, L., Bai, B., and Yu, B. (2022). Investigation of thermal-hydro-mechanical coupled fracture propagation considering rock damage. *Computational Geosciences*, 26(5):1167–1187.

Kaya, E., Zarrouk, S. J., and O'Sullivan, M. J. (2011). Reinjection in geothermal fields: A review of worldwide experience. *Renewable and sustainable energy reviews*, 15(1):47–68.

Kumari, W., Ranjith, P., Perera, M., Li, X., Li, L., Chen, B., Isaka, B. A., and De Silva, V. (2018). Hydraulic fracturing under high temperature and pressure conditions with micro ct applications: geothermal energy from hot dry rocks. *Fuel*, 230:138–154.

Lee, T., Park, D., Shin, C., Jeong, D., and Choe, J. (2016). Efficient production estimation for a hydraulic fractured well considering fracture closure and proppant placement effects. *Energy Exploration & Exploitation*, 34(4):643–658.

Li, N., Ma, X., Zhang, S., Zou, Y., Wu, S., Li, S., Zhang, Z., and Cao, T. (2020). Thermal effects on the physical and mechanical properties and fracture initiation of laizhou granite during hydraulic fracturing. *Rock Mechanics and Rock Engineering*, 53:2539–2556.

Li, N., Zhang, S., Wang, H., Ma, X., Zou, Y., and Zhou, T. (2021a). Effect of thermal shock on laboratory hydraulic fracturing in laizhou granite: An experimental study. *Engineering Fracture Mechanics*, 248:107741.

Li, P., Li, D., Wang, Q., and Zhou, K. (2021b). Phase-field modeling of hydro-thermally induced fracture in thermo-poroelastic media. *Engineering Fracture Mechanics*, 254:107887.

Li, S., Li, X., and Zhang, D. (2016a). A fully coupled thermo-hydro-mechanical, three-dimensional model for hydraulic stimulation treatments. *Journal of Natural Gas Science and Engineering*, 34:64–84.

Li, T., Marigo, J.-J., Guilbaud, D., and Potapov, S. (2016b). Gradient damage modeling of brittle fracture in an explicit dynamics context. *International Journal for Numerical Methods in Engineering*, 108(11):1381–1405.

Li, W., Soliman, M., and Han, Y. (2016c). Microscopic numerical modeling of thermo-hydro-mechanical mechanisms in fluid injection process in unconsolidated formation. *Journal of Petroleum Science and Engineering*, 146:959–970.

Li, X., Li, G., Yu, W., Wang, H., Sepehrnoori, K., Chen, Z., Sun, H., and Zhang, S. (2018). Thermal effects of liquid/supercritical carbon dioxide arising from fluid expansion in fracturing. *SPE Journal*, 23(06):2026–2040.

Lima, M. G., Vogler, D., Querci, L., Madonna, C., Hattendorf, B., Saar, M. O., and Kong, X.-Z. (2019). Thermally driven fracture aperture variation in naturally fractured granites. *Geothermal Energy*, 7:1–28.

Liu, X., Wang, Y., Li, S., Jiang, X., and Fu, W. (2020a). The influence of reinjection and hydrogeological parameters on thermal energy storage in brine aquifer. *Applied Energy*, 278:115685.

Liu, Y., Yoshioka, K., You, T., Li, H., and Zhang, F. (2024). A phase-field fracture model in thermo-poro-elastic media with micromechanical strain energy degradation. *Computer Methods in Applied Mechanics and Engineering*, 429:117165.

Liu, Z., Sun, Y., Guo, W., and Li, Q. (2020b). Reservoir-scale study of oil shale hydration swelling and thermal expansion after hydraulic fracturing. *Journal of Petroleum Science and Engineering*, 195:107619.

Magri, F., Cacace, M., Fischer, T., Kolditz, O., Wang, W., and Watanabe, N. (2017). Thermal convection of viscous fluids in a faulted system: 3D benchmark for numerical codes. *Energy Procedia*, 125:310–317.

Manchanda, R., Zheng, S., Gala, D., and Sharma, M. (2019). Simulating the life of hydraulically fractured wells using a fully-coupled poroelastic fracture-reservoir simulator. In *SPE/AAPG/SEG Unconventional Resources Technology Conference*, page D023S052R007. URTEC.

Martins, J., Murray, L., Clifford, P., McLelland, W., Hanna, M., and Sharp Jr, J. (1995). Produced-water reinjection and fracturina in prudhoe bay. *SPE Reservoir Engineering*, 10(03):176–182.

Mesgarnejad, A., Bourdin, B., and Khonsari, M. (2015). Validation simulations for the variational approach to fracture. *Computer Methods in Applied Mechanics and Engineering*, 290:420–437.

Miehe, C., Hofacker, M., and Welschinger, F. (2010). A phase field model for rate-independent crack propagation: Robust algorithmic implementation based on operator splits. *Computer Methods in Applied Mechanics and Engineering*, 199(45-48):2765–2778.

Miehe, C. and Mauthe, S. (2016). Phase field modeling of fracture in multi-physics problems. part III. crack driving forces in hydro-poro-elasticity and hydraulic fracturing of fluid-saturated porous media. *Computer Methods in Applied Mechanics and Engineering*, 304:619–655.

Miehe, C., Mauthe, S., and Teichtmeister, S. (2015). Minimization principles for the coupled problem of darcy–biot-type fluid transport in porous media linked to phase field modeling of fracture. *Journal of the Mechanics and Physics of Solids*, 82:186–217.

Mikelić, A., Wheeler, M. F., and Wick, T. (2015). A quasi-static phase-field approach to pressurized fractures. *Nonlinearity*, 28(5):1371.

Noii, N. and Wick, T. (2019). A phase-field description for pressurized and non-isothermal propagating fractures. *Computer Methods in Applied Mechanics and Engineering*, 351:860–890.

Parisio, F., Vilarrasa, V., Wang, W., Kolditz, O., and Nagel, T. (2019). The risks of long-term re-injection in supercritical geothermal systems. *Nature communications*, 10(1):4391.

Parisio, F. and Yoshioka, K. (2020). Modeling fluid reinjection into an enhanced geothermal system. *Geophysical Research Letters*, 47(19):e2020GL089886.

Perkins, T. and Gonzalez, J. (1985). The effect of thermoelastic stresses on injection well fracturing. *Society of Petroleum Engineers Journal*, 25(01):78–88.

Petrova, V. and Schmauder, S. (2015). Crack closure effects in thermal fracture of functionally graded/homogeneous bimaterials with systems of cracks. *ZAMM-Journal of Applied Mathematics and Mechanics/Zeitschrift für Angewandte Mathematik und Mechanik*, 95(10):1027–1036.

Pham, K., Amor, H., Marigo, J.-J., and Maurini, C. (2011). Gradient damage models and their use to approximate brittle fracture. *International Journal of Damage Mechanics*, 20(4):618–652.

Qu, Z.-Q., Zhang, W., and Guo, T.-k. (2017). Influence of different fracture morphology on heat mining performance of enhanced geothermal systems based on comsol. *International journal of hydrogen energy*, 42(29):18263–18278.

Ran, L., Sirui, P., Jinzhou, Z., Hao, J., Lan, R., Bo, Z., Jianfa, W., Yi, S., and Cheng, S. (2024). Multiple hydraulic fracture propagation simulation in deep shale gas reservoir considering thermal effects. *Engineering Fracture Mechanics*, page 110147.

Rutqvist, J., Rinaldi, A. P., Cappa, F., and Moridis, G. J. (2013). Modeling of fault reactivation and induced seismicity during hydraulic fracturing of shale-gas reservoirs. *Journal of Petroleum Science and Engineering*, 107:31–44.

Sacco, E. (1990). Modellazione e calcolo di strutture in materiale non resistente a trazione. *Atti della Accademia Nazionale dei Lincei. Classe di Scienze Fisiche, Matematiche e Naturali. Rendiconti Lincei. Matematica e Applicazioni*, 1(3):235–258.

Schroeder, R. C., O'Sullivan, M. J., Pruess, K., Celati, R., and Ruffilli, C. (1982). Reinjection studies of vapor-dominated systems. *Geothermics*, 11(2):93–119.

Sheng, J. J. (2014). Critical review of low-salinity waterflooding. *Journal of Petroleum Science and Engineering*, 120:216–224.

Shi, H., Wang, G., and Lu, C. (2023). Numerical investigation on delaying thermal breakthrough by regulating reinjection fluid path in multi-aquifer geothermal system. *Applied Thermal Engineering*, 221:119692.

Shu, B., Zhu, R., Elsworth, D., Dick, J., Liu, S., Tan, J., and Zhang, S. (2020). Effect of temperature and confining pressure on the evolution of hydraulic and heat transfer properties of geothermal fracture in granite. *Applied Energy*, 272:115290.

Silhavy, M. (1997). *The mechanics and thermodynamics of continuous media*. Springer Science & Business Media.

Stefansson, V.-d. (1997). Geothermal reinjection experience. *Geothermics*, 26(1):99–139.

Stephens, G. and Voight, B. (1982). Hydraulic fracturing theory for conditions of thermal stress. In *International Journal of Rock Mechanics and Mining Sciences & Geomechanics Abstracts*, volume 19, pages 279–284. Elsevier.

Suh, H. S. and Sun, W. (2021). Asynchronous phase field fracture model for porous media with thermally non-equilibrated constituents. *Computer Methods in Applied Mechanics and Engineering*, 387:114182.

Sun, J., Liu, Q., and Duan, Y. (2019). Effects of reinjection temperature on thermodynamic performance of dual-pressure and single-pressure geothermal orcs. *Energy Procedia*, 158:6016–6023.

Tanné, E., Li, T., Bourdin, B., Marigo, J.-J., and Maurini, C. (2018). Crack nucleation in variational phase-field models of brittle fracture. *Journal of the Mechanics and Physics of Solids*, 110:80–99.

Tarasovs, S. and Ghassemi, A. (2011). Propagation of a system of cracks under thermal stress. In *ARMA US Rock Mechanics/Geomechanics Symposium*, pages ARMA–11. ARMA.

Tomac, I. and Gutierrez, M. (2017). Coupled hydro-thermo-mechanical modeling of hydraulic fracturing in quasi-brittle rocks using bpm-dem. *Journal of Rock Mechanics and Geotechnical Engineering*, 9(1):92–104.

Wang, W., Kosakowski, G., and Kolditz, O. (2009). A parallel finite element scheme for thermo-hydro-mechanical (thm) coupled problems in porous media. *Computers & Geosciences*, 35(8):1631–1641.

Wang, X., Li, P., Qi, T., Li, L., Li, T., Jin, J., and Lu, D. (2023). A framework to model the hydraulic fracturing with thermo-hydro-mechanical coupling based on the variational phase-field approach. *Computer Methods in Applied Mechanics and Engineering*, 417:116406.

Wassing, B., Van Wees, J., and Fokker, P. (2014). Coupled continuum modeling of fracture reactivation and induced seismicity during enhanced geothermal operations. *Geothermics*, 52:153–164.

Wei, S.-M., Xia, Y., Jin, Y., Guo, X.-Y., Zi, J.-Y., Qiu, K.-X., and Chen, S.-Y. (2024). Production induced fracture closure of deep shale gas well under thermo-hydro-mechanical conditions. *Petroleum Science*, 21(3):1796–1813.

Wheeler, M. F., Wick, T., and Wollner, W. (2014). An augmented-lagrangian method for the phase-field approach for pressurized fractures. *Computer Methods in Applied Mechanics and Engineering*, 271:69–85.

Yan, C., Xie, X., Ren, Y., Ke, W., and Wang, G. (2022). A fdem-based 2d coupled thermal-hydro-mechanical model for multiphysical simulation of rock fracturing. *International Journal of Rock Mechanics and Mining Sciences*, 149:104964.

Yi, D., Yi, L., Yang, Z., Meng, Z., Li, X., Yang, C., and Zhang, D. (2024). Coupled thermo-hydro-mechanical-phase field modelling for hydraulic fracturing in thermo-poroelastic media. *Computers and Geotechnics*, 166:105949.

Yoshioka, K., Parisio, F., Naumov, D., Lu, R., Kolditz, O., and Nagel, T. (2019a). Comparative verification of discrete and smeared numerical approaches for the simulation of hydraulic fracturing. *GEM-International Journal on Geomathematics*, 10:1–35.

Yoshioka, K., Pasikki, R., and Stimac, J. (2019b). A long term hydraulic stimulation study conducted at the Salak geothermal field. *Geothermics*, 82:168–181.

You, T. and Yoshioka, K. (2023). On poroelastic strain energy degradation in the variational phase-field models for hydraulic fracture. *Computer Methods in Applied Mechanics and Engineering*, 416:116305.

Zang, A., Oye, V., Jousset, P., Deichmann, N., Gritto, R., McGarr, A., Majer, E., and Bruhn, D. (2014). Analysis of induced seismicity in geothermal reservoirs–an overview. *Geothermics*, 52:6–21.

Zhang, Y.-J., Guo, L.-L., Li, Z.-W., Yu, Z.-W., Xu, T.-F., and Lan, C.-Y. (2015). Electricity generation and heating potential from enhanced geothermal system in songliao basin, china: Different reservoir stimulation strategies for tight rock and naturally fractured formations. *Energy*, 93:1860–1885.

Zhou, C., Wan, Z., Zhang, Y., and Gu, B. (2018). Experimental study on hydraulic fracturing of granite under thermal shock. *Geothermics*, 71:146–155.

Zhou, Z., Mikada, H., Takekawa, J., and Xu, S. (2022). Numerical simulation of hydraulic fracturing in enhanced geothermal systems considering thermal stress cracks. *Pure and Applied Geophysics*, 179(5):1775–1804.

Zhuang, X., Zhou, S., Huynh, G., Areias, P., and Rabczuk, T. (2022). Phase field modeling and computer implementation: A review. *Engineering Fracture Mechanics*, 262:108234.